

Enhancement of transverse thermoelectric conductivity originating from stationary points in nodal lines

Susumu Minami* and Fumiyuki Ishii†

Nanomaterials Research Institute (NanoMaRi), Kanazawa University, Kakuma, Kanazawa, 920-1192, Japan

Motoaki Hirayama

Center for Emergence Matter Science (CEMS), RIKEN, Hirosawa, Wako, Saitama 351-0198, Japan

Takuya Nomoto

Department of Applied Physics, The University of Tokyo, Hongo, Bunkyo-ku, Tokyo, 113-8656, Japan

Takashi Koretsune

Department of Physics, Tohoku University, Sendai, Miyagi, 980-8578, Japan

Ryotaro Arita

*Center for Emergence Matter Science (CEMS), RIKEN, Hirosawa, Wako, Saitama 351-0198, Japan and
Department of Applied Physics, The University of Tokyo, Hongo, Bunkyo-ku, Tokyo, 113-8656, Japan*

(Dated: August 31, 2020)

Motivated by the recent discovery of a large anomalous Nernst effect in Co_2MnGa , Fe_3X ($X=\text{Al}$, Ga) and $\text{Co}_3\text{Sn}_2\text{S}_2$, we performed a first-principles study to clarify the origin of the enhancement of the transverse thermoelectric conductivity (α_{ij}) in these ferromagnets. The intrinsic contribution to α_{ij} can be understood in terms of the Berry curvature (Ω) around the Fermi level, and Ω is singularly large along nodal lines (which are gapless in the absence of the spin-orbit coupling) in the Brillouin zone. We find that not only the Weyl points but also stationary points in the energy dispersion of the nodal lines play a crucial role. The stationary points make sharp peaks in the density of states projected onto the nodal line, clearly identifying the characteristic Fermi energies at which α_{ij} is most dramatically enhanced. We also find that α_{ij}/T breaks the Mott relation and show a peculiar temperature dependence at these energies. The present results suggest that the stationary points will give us a useful guiding principle to design magnets showing a large anomalous Nernst effect.

I. INTRODUCTION

In solids, a temperature gradient (∇T) and an external electric field (\mathbf{E}) gives rise to a charge current (\mathbf{J}) given as

$$\mathbf{J} = \hat{\sigma}\mathbf{E} + \hat{\alpha}(-\nabla T), \quad (1)$$

where $\hat{\sigma}$ and $\hat{\alpha}$ are the electric conductivity tensor and thermoelectric (TE) tensor, respectively. When \mathbf{J} is absent, eq. (1) tells us that a temperature gradient generates a voltage as

$$\mathbf{E} = \hat{S}(\nabla T),$$

where $\hat{S} = \hat{\sigma}^{-1}\hat{\alpha}$. In ferromagnets, off diagonal elements of $\hat{\sigma}$ and $\hat{\alpha}$ are generally finite, so that a transverse voltage is induced by a longitudinal temperature gradient. This phenomenon is a thermoelectric counterpart of the anomalous Hall effect (AHE) and called the anomalous Nernst effect (ANE)¹⁻³.

Recently, the ANE is attracting renewed interest. It can be exploited in developing high-efficiency energy-harvesting devices with simple lateral structure, high flexibility and low production cost^{4,5}. Experimental and theoretical studies of AHE⁶⁻¹⁷ and ANE¹⁸⁻³⁹ have been reported in a variety of magnetic materials. Among them, Co_2MnGa ^{18,19}, Fe_3X ($X=\text{Al}$, Ga)²⁰ and

$\text{Co}_3\text{Sn}_2\text{S}_2$ ²¹⁻²³ are of particular interest due to their huge anomalous transverse transport and less entangled low-energy electronic structure.

In fact, if the band dispersion around the Fermi level (E_F) is not so complicated, there is an intriguing possibility to design a giant ANE. This is because the transverse thermoelectric conductivity is directly related to the Berry curvature (Ω) of the low-energy bands, which can be calculated from first principles accurately³:

$$\sigma_{ij}(T, \mu) = -\varepsilon_{ijl} \frac{e^2}{\hbar} \int \frac{d\mathbf{k}}{(2\pi)^3} \sum_m \Omega_{m,l}(\mathbf{k}) f(\varepsilon_{m\mathbf{k}}), \quad (2)$$

$$\alpha_{ij}(T, \mu) = -\frac{1}{e} \int d\varepsilon \sigma_{ij}(0, \varepsilon) \frac{\varepsilon - \mu}{T} \left(-\frac{\partial f}{\partial \varepsilon} \right), \quad (3)$$

where ε_{ijl} , e , \hbar , ε , f , μ are the antisymmetric tensor, elementary charge with negative sign, the reduced Planck constant, the band energy, the Fermi-Dirac distribution function with the band index m and the wave vector \mathbf{k} , and the chemical potential, respectively. The Berry curvature for the m -th band is given as

$$\Omega_{m,l}(\mathbf{k}) = -2\varepsilon_{ijl} \text{Im} \sum_{m' \neq m} \frac{v_{mm',i}(\mathbf{k})v_{m'm,j}(\mathbf{k})}{(\varepsilon_{m'}(\mathbf{k}) - \varepsilon_m(\mathbf{k}))^2}, \quad (4)$$

where $v_{mm',i}$ denotes the matrix elements of the velocity operator along the i direction, respectively.

In non-relativistic calculation, we generally find many nodal lines in the Brillouin zone. The nodal line is a one-dimensional topological degeneracy where the energy gap closes^{40–48}. The spin-orbit coupling (SOC) opens a small gap along these nodal lines and the Berry curvature is singularly large there because the energy difference $|\varepsilon_{m'} - \varepsilon_m|$ is small (see eq. (4)). In particular, the Berry curvature diverges at the Weyl points, at which the band crossing survives even in the presence of the SOC. Therefore, the existence of the nodal lines and especially the Weyl points around E_F has been considered to be critically important for realizing large anomalous transverse transport. Indeed, the role of various topological objects such as the type-II Weyl point⁴⁹ and Hopf link of nodal lines have been extensively studied for Heusler ferromagnets^{16–20,29,50,51}, $\text{Co}_3\text{Sn}_2\text{S}_2$ ^{21–23}, and other ferromagnets^{52–55}. However, there is no established general guiding principle to design magnets showing a large ANE.

In this paper, we propose that stationary points in the energy dispersion of nodal lines play a crucial role to determine the best energy for μ at which the ANE is most dramatically enhanced. The nodal lines are one-dimensional objects in the Brillouin zone, so that the stationary points make sharp peaks in the density of states (DOS) projected onto the nodal lines:

$$D_{\text{NL}}(\varepsilon) = \sum_{n, \mathbf{k} \in \mathbf{k}_{\text{NL}}} \delta(\varepsilon - \varepsilon_{n\mathbf{k}}),$$

where n is the band index and \mathbf{k}_{NL} specifies the positions of the nodal lines. Based on first-principles calculations for Co_2MnGa , Fe_3Al and $\text{Co}_3\text{Sn}_2\text{S}_2$, we show that there is a clear one-to-one correspondence between the “van Hove singularities” in the $D_{\text{NL}}(\varepsilon = E_{\text{VHS}})$ and the energy for μ at which the transverse TE conductivity is enhanced.

When μ is located at E_{VHS} , we can also find a breakdown of the Mott relation as a prominent indication of the enhancement of the transverse TE conductivity. The Mott relation is derived by using the Sommerfeld expansion for eq. (3), which is usually valid at sufficient low temperatures^{32,33,56–61}.

$$\alpha_{ij}(T, \mu) = -\frac{\pi^2 k_{\text{B}}^2 T}{3|e|} \left. \frac{d\sigma_{ij}(0, \varepsilon)}{d\varepsilon} \right|_{\varepsilon=E_F},$$

where k_{B} is the Boltzmann constant. Thus for many materials, α_{ij}/T is a constant at $T \rightarrow 0$. However, recently, it has been found that α_{ij}/T diverges at low temperatures in several ferromagnets which exhibit a large ANE^{1,18,20–22,24,25}. We show that this peculiar behavior can be understood in terms of D_{NL} : The energy dependence of $\sigma_{ij}(0, \varepsilon)$ is singular at $\varepsilon = E_{\text{VHS}}$ where D_{NL} has a sharp peak. There, the Sommerfeld expansion does not work even at low temperatures. We show that the Mott relation is indeed violated for Co_2MnGa , Fe_3Al and $\text{Co}_3\text{Sn}_2\text{S}_2$, when μ is close to E_{VHS} and the transverse TE conductivity is strongly enhanced.

TABLE I. Space group, lattice constant (a, c), and Curie temperature (T_C) of each material. Our calculations were performed using the experimental lattice constants.

M	space group	a, c (Å)	T_C (K)
Co_2MnGa	$Fm\bar{3}m$	5.77 ^a	694 ^b
$\text{Co}_3\text{Sn}_2\text{S}_2$	$R\bar{3}m$	$a = 5.36, c = 13.17$ ^c	177 ^d
Fe_3Al	$Fm\bar{3}m$	5.79 ^e	760 ^e

^a Ref. [18]

^b Ref. [62]

^c Ref. [21]

^d Ref. [63]

^e Ref. [64]

II. COMPUTATIONAL DETAILS

We conducted first-principles calculations based on the non-collinear density functional theory⁶⁵ (DFT) with OPENMX code⁶⁶. DFT calculations are performed through the exchange-correlation functional within the generalized-gradient approximation and norm-conserving pseudopotentials⁶⁷. The SOC is included by using total angular momentum dependent pseudopotentials⁶⁸. The wave functions are expanded by a linear combination of multiple pseudo-atomic orbitals⁶⁹. A set of pseudoatomic orbital basis was specified as Al17.0- $s3p3d1$, S7.0- $s3p3d1$, Mn6.0- $s3p3d3$, Fe6.0- $s3p3d3$, Co6.0- $s3p3d3$, Ga7.0- $s3p3d3$, and Sn7.0- $s3p3d1$ where the number after each element stands for the radial cutoff in the unit of bohr and the integer after s, p, d indicates the radial multiplicity of each angular momentum component. The cutoff energy for charge density of 800 Ry and a k -point mesh of $35 \times 35 \times 35$ were used. The nodal lines were obtained by monitoring the degeneracy of eigenvalues in the momentum space based on electronic structure without SOC⁷⁰. Table I shows the space group, lattice constant, and Curie temperature of each material. The lattice constants of each material refer to the experimental ones as listed in Table I.

From the Bloch states obtained in the DFT calculation, a Wannier basis set was constructed by using the WANNIER90 code⁷¹. The basis was composed of (s, p)-character orbitals localized at the Al and S site, d -character orbitals at the Co, Mn and Fe site, p -character orbitals at the Ga and Sn site. Therefore, we consider 36 orbitals/f.u. for Co_2MnGa , 62 orbitals/f.u. for $\text{Co}_3\text{Sn}_2\text{S}_2$, 38 orbitals/f.u. for Fe_3Al including the spin multiplicity. These sets were extracted from 194, 102 and 92 bands in the energy window ranging from -20 eV to $+50$ eV, -15 eV to $+40$ eV, and -15 eV to $+50$ eV for $\text{Co}_3\text{Sn}_2\text{S}_2$, Co_2MnGa , and Fe_3Al , respectively.

The anomalous Hall conductivity (eq. (2)) and the anomalous transverse TE conductivity (eq. (3)) at finite temperature were computed with the WANNIER90 code using a k -point mesh of $100 \times 100 \times 100$ and additionally an adaptive mesh of $3 \times 3 \times 3$ for regions with large $\Omega_{n,l}$.

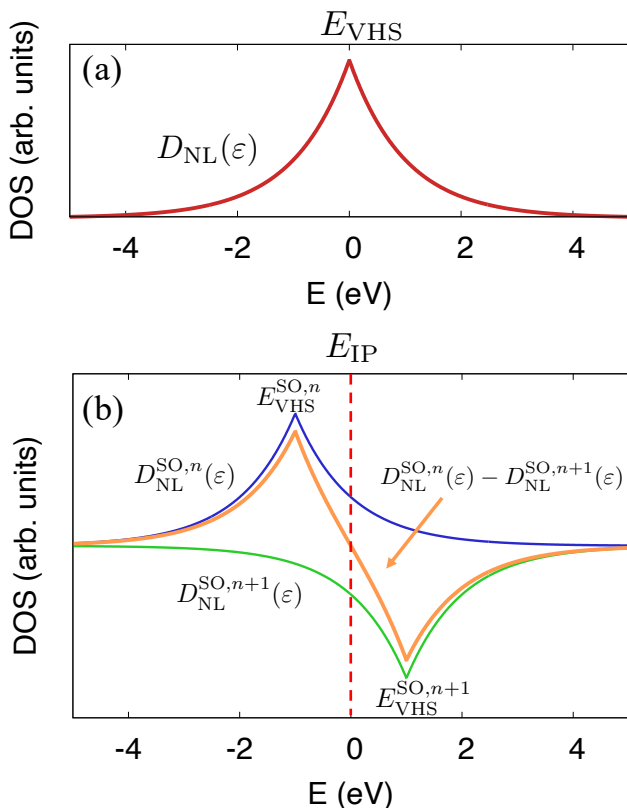


FIG. 1. Schematic of (a) $D_{\text{NL}}(\varepsilon)$ without SOC and (b) $D_{\text{NL}}^{\text{SO},n}$, $-D_{\text{NL}}^{\text{SO},n+1}$ with SOC and $D_{\text{NL}}^{\text{SO},n} - D_{\text{NL}}^{\text{SO},n+1}$ in eq (10).

III. RESULTS AND DISCUSSION

A. Enhancement of transverse thermoelectric conductivity and violation of the Mott relation

Let us first discuss how the van Hove singularities in D_{NL} cause the enhancement of the transverse TE conductivity and breakdown of the Mott relation. Equation (3) can be rewritten as¹

$$\alpha_{ij} = \frac{k_{\text{B}}}{e} \int d\varepsilon \frac{\partial \sigma_{ij}}{\partial \varepsilon} s(\varepsilon, T), \quad (5)$$

$$\frac{\partial \sigma_{ij}}{\partial \varepsilon} = \varepsilon_{ijl} \sum_{n\mathbf{k}} \Omega_{n,l}(\mathbf{k}) \delta(\varepsilon - \varepsilon_{n\mathbf{k}}), \quad (6)$$

$$s = -f \ln(f) - (1-f) \ln(1-f), \quad (7)$$

where $s(\varepsilon, T)$ is the entropy density.

For eq. (6), let us introduce the following approximation: In the presence of the SOC, the absolute value of the Berry curvature $\Omega_{n,l}(\mathbf{k})$ is large at \mathbf{k} where the effect of the SOC on $\varepsilon_{n\mathbf{k}}$ is prominent. Thus $|\Omega_{n,l}(\mathbf{k})|$ takes a large value on nodal lines in the non-relativistic calculation for which the SOC opens a gap. Suppose that the n -th and $n+1$ -th band make nodal lines (at $\mathbf{k} \in \mathbf{k}_{\text{NL}}$) in the absence of the SOC and consider the density of states $D_{\text{NL}}(\varepsilon)$ for these band crossing points. The SOC splits $D_{\text{NL}}(\varepsilon)$ into the DOS for the n -th band ($D_{\text{NL}}^{\text{SO},n}(\varepsilon)$)

and $n+1$ -th band ($D_{\text{NL}}^{\text{SO},n+1}(\varepsilon)$). Since $|\Omega_{n,l}(\mathbf{k})|$ is small at ordinary \mathbf{k} points that are not on the nodal lines (i.e., $\mathbf{k} \notin \mathbf{k}_{\text{NL}}$),

$$\frac{\partial \sigma_{ij}}{\partial \varepsilon} \sim \Omega_{\text{NL}}^n(\varepsilon) D_{\text{NL}}^{\text{SO},n}(\varepsilon) + \Omega_{\text{NL}}^{n+1}(\varepsilon) D_{\text{NL}}^{\text{SO},n+1}(\varepsilon). \quad (8)$$

Here, $\Omega_{\text{NL}}^n(\varepsilon)$ denotes the averaged value of the Berry curvature on the nodal line,

$$\Omega_{\text{NL}}^n(\varepsilon) = \sum_{\mathbf{k} \in \mathbf{k}_{\text{NL}}} \Omega_{n,l}(\mathbf{k}) \delta(\varepsilon - \varepsilon_{n\mathbf{k}}) / \sum_{\mathbf{k} \in \mathbf{k}_{\text{NL}}} \delta(\varepsilon - \varepsilon_{n\mathbf{k}}). \quad (9)$$

When \mathbf{k} is on the nodal line formed by the n -th and $n+1$ -th band, the contribution of $m = n$, $m' = n+1$ is prevailing in Eq. (4) for $\Omega_{n,l}(\mathbf{k})$ since the factor of $1/(\varepsilon_{n\mathbf{k}} - \varepsilon_{n+1\mathbf{k}})^2$ is dominantly large. Similarly for $\Omega_{n+1,l}(\mathbf{k})$, the contribution of $m = n+1$, $m' = n$ is dominant. Thus, if we assume $\varepsilon_{n\mathbf{k}} \sim \varepsilon_{n+1\mathbf{k}}$, then $\Omega_{\text{NL}}^n(\varepsilon) \sim -\Omega_{\text{NL}}^{n+1}(\varepsilon)$, and eq. (8) can be further approximated as

$$\frac{\partial \sigma_{ij}}{\partial \varepsilon} \sim \Omega_{\text{NL}}^n(\varepsilon) (D_{\text{NL}}^{\text{SO},n}(\varepsilon) - D_{\text{NL}}^{\text{SO},n+1}(\varepsilon)). \quad (10)$$

We illustrate a schematic of D_{NL} with and without SOC in Fig. 1. Since D_{NL} is essentially the DOS of one-dimensional objects, it has sharp peaks (“van Hove singularities”) at the energies of stationary points (i.e., $\varepsilon = E_{\text{VHS}}$) in the nodal lines as shown in Fig. 1(a). In the presence of the SOC, $D_{\text{NL}}^{\text{SO},n}$ and $D_{\text{NL}}^{\text{SO},n+1}$ also have sharp peaks at $\varepsilon = E_{\text{VHS}}^{\text{SO},n}$, $E_{\text{VHS}}^{\text{SO},n+1}$ as shown in Fig. 1(b). Since $s_{n\mathbf{k}}$ takes a maximum around $\varepsilon = E_{\text{F}}$, we see that α_{ij} will be enhanced when $E_{\text{VHS}}^{\text{SO},n} = E_{\text{F}}$ (see eq. (5)).

As we have seen in eq. (10), $\partial \sigma_{ij} / \partial \varepsilon$ is approximately proportional to the difference between $D_{\text{NL}}^{\text{SO},n}(\varepsilon)$ and $D_{\text{NL}}^{\text{SO},n+1}(\varepsilon)$ (See Fig. 1(b)). Thus we expect that α_{ij} takes its maximum or minimum at $E_{\text{VHS}}^{\text{SO},n}$ ($E_{\text{VHS}}^{\text{SO},n+1}$) in $D_{\text{NL}}^{\text{SO},n}(\varepsilon)$ ($D_{\text{NL}}^{\text{SO},n+1}(\varepsilon)$). On the other hand, E_{VHS} in $D_{\text{NL}}(\varepsilon)$ is located between those in $D_{\text{NL}}^{\text{SO},n}(\varepsilon)$ and $D_{\text{NL}}^{\text{SO},n+1}(\varepsilon)$. Therefore, E_{VHS} in $D_{\text{NL}}(\varepsilon)$ is expected to reside between the minimum and maximum in α_{ij} . Namely, E_{VHS} in $D_{\text{NL}}(\varepsilon)$ corresponds to the “inflection point” in α_{ij} and gives crucial information to identify the chemical potential at which α_{ij} is substantially enhanced.

We can further show that if $D_{\text{NL}}^{\text{SO},n}$ or $D_{\text{NL}}^{\text{SO},n+1}$ has a logarithmic singularity at $\varepsilon = E_{\text{VHS}}$ and $E_{\text{VHS}} = E_{\text{F}}$, $\alpha_{ij}/T = c_1 \ln T + c_2$. Similarly, if $D_{\text{NL}}^{\text{SO},n}(\varepsilon)$ or $D_{\text{NL}}^{\text{SO},n+1}(\varepsilon)$ is proportional to $(\varepsilon - E_{\text{VHS}})^m$, $\alpha/T = c_3 T^m$. Here, c_1 , c_2 and c_3 are constants which do not depend on T . In Ref. [18], it has been proposed that when the Weyl fermions reside close to the Lifshitz transition from the type-I to type-II, $\partial \sigma_{ij} / \partial \varepsilon$ has a logarithmic divergence, which leads a quantum critical behavior of the transverse TE conductivity. Our present discussion is a generalization of this result.

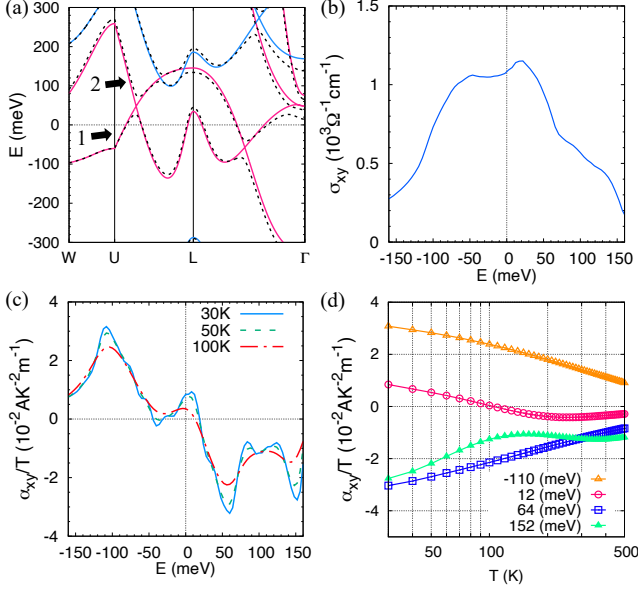


FIG. 2. (a) Band structure of $\text{Co}_3\text{Sn}_2\text{S}_2$. Pink and cyan lines correspond to the majority and minority spin bands computed without SOC. Dashed lines show the band calculated including SOC. The denoted majority bands 1, and 2 make the nodal line. (b) μ dependence of σ_{xy} at 0 K. (c) μ dependence of α_{xy}/T . Solid, dotted, and dash-dotted line are the results for $T = 30, 50, \text{ and } 100\text{K}$, respectively. (d) T dependence of α_{xy}/T . Open triangle, open circle, open square and solid triangle line correspond to the results for $\mu = -110, 12, 64, \text{ and } 152\text{ meV}$, respectively.

B. Magnetic Weyl semimetal $\text{Co}_3\text{Sn}_2\text{S}_2$

Let us now look into the first-principles calculation for the magnetic Weyl semimetal $\text{Co}_3\text{Sn}_2\text{S}_2$, which has simple electronic structure composed of Weyl points and nodal line near the E_F . Figure 2 shows the band structure, μ dependence of σ_{xy} and α_{xy}/T , and T dependence of α_{xy}/T . The obtained total magnetic moment is $0.9 \mu_B/\text{f.u.}$ so that spin polarization per each Co atom is $0.3 \mu_B$. The calculated σ_{xy} at E_F is $1093 \Omega^{-1}\text{cm}^{-1}$, which is consistent with the previous theoretical calculation ($1100 \Omega^{-1}\text{cm}^{-1}$) and the experimental value ($1130 \Omega^{-1}\text{cm}^{-1}$) [21]. Figures 2(c) and (d) show that α_{xy}/T is enhanced and has a peculiar temperature dependence at $\mu = -110, 12, 64$ and 152 meV . Namely, α_{xy}/T does not satisfy the Mott relation at these energies.

As is seen in Fig. 2(a), the low-energy electronic structure of $\text{Co}_3\text{Sn}_2\text{S}_2$ is very simple: Only the majority spin contributes to the Fermi surface and there is only one nodal line formed by band 1 and band 2 in Fig. 2(a).

Let us next discuss the enhancement of α_{ij} and the violation of the Mott relation in terms of the nodal line. In Fig. 3(a), we show the nodal line in the Brillouin zone. We can see that the “band width” of the nodal line is about 240 meV , and the nodal line appears on the high symmetry planes. Figures 3(b) and 3(c) show the energy

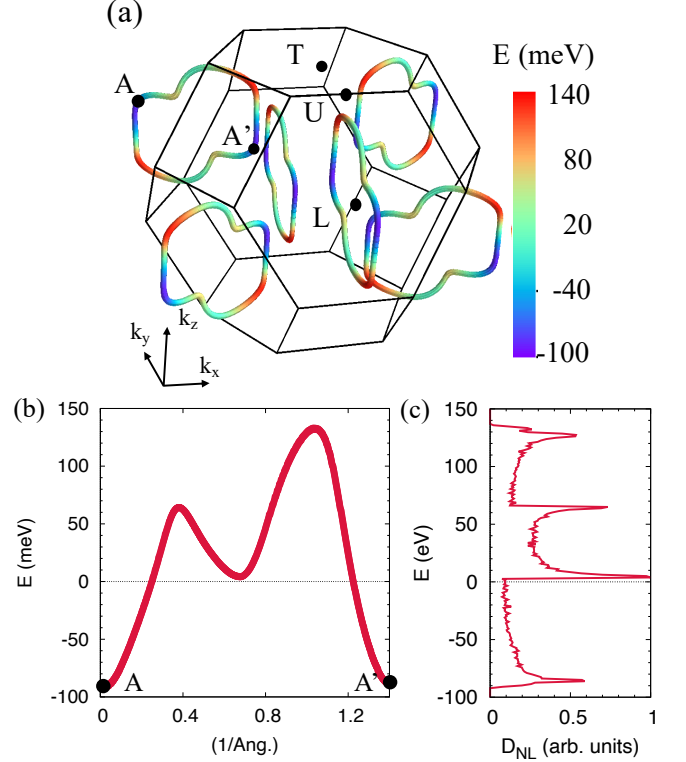


FIG. 3. (a) Nodal line network of $\text{Co}_3\text{Sn}_2\text{S}_2$. The color bar corresponds to the energy range from -100 to 140 meV . (b) Energy dispersion along the nodal line and (c) D_{NL} for $\text{Co}_3\text{Sn}_2\text{S}_2$. The A and A' point are shown in Fig. 3(a).

dispersion along the nodal line (the “nodal-line band”) and D_{NL} for $\text{Co}_3\text{Sn}_2\text{S}_2$, respectively. We chose the k -path along the nodal line in Fig. 3(a), where the positions of the A and A' are indicated. Due to the symmetry of the Brillouin zone, there are two periods of changes in the Berry curvature in one loop of the nodal line. The nodal-line band in Fig. 3(b) have one maximum, one minimum and two other stationary points. The energies of these points have a one-to-one correspondence with the van Hove singularities in D_{NL} (Fig. 3(b)).

Figure 4 shows the μ dependence of D_{NL} and $D_{\text{NL}}^{\text{SO},n}$, $D_{\text{NL}}^{\text{SO},n+1}$ and $D_{\text{NL}}^{\text{SO},n} - D_{\text{NL}}^{\text{SO},n+1}$, and α_{xy}/T . In Fig. 4(a), we see that four sharp peaks in D_{NL} . In Fig. 4(b), we plot $D_{\text{NL}}^{\text{SO},n}$, $-D_{\text{NL}}^{\text{SO},n+1}$, and $D_{\text{NL}}^{\text{SO},n} - D_{\text{NL}}^{\text{SO},n+1}$ and compare the energies of the van Hove singularities (E_{VHS} 's). In Fig. 4(c), we see that the peaks in $D_{\text{NL}}^{\text{SO},n}$ and $-D_{\text{NL}}^{\text{SO},n+1}$ correspond to the energies at which α_{xy}/T takes its maximum and minimum, respectively. These peaks originate from the “van Hove singularities”, i.e., the stationary points in the energy dispersion of the nodal lines. We see that each E_{VHS} in D_{NL} is located between those in $D_{\text{NL}}^{\text{SO},n+1}$ and $D_{\text{NL}}^{\text{SO},n}$. Therefore, each E_{VHS} in D_{NL} corresponds to the “inflection point” between the maximum and minimum in α_{xy}/T .

In Table II, we compare the inflection point in α_{xy}/T

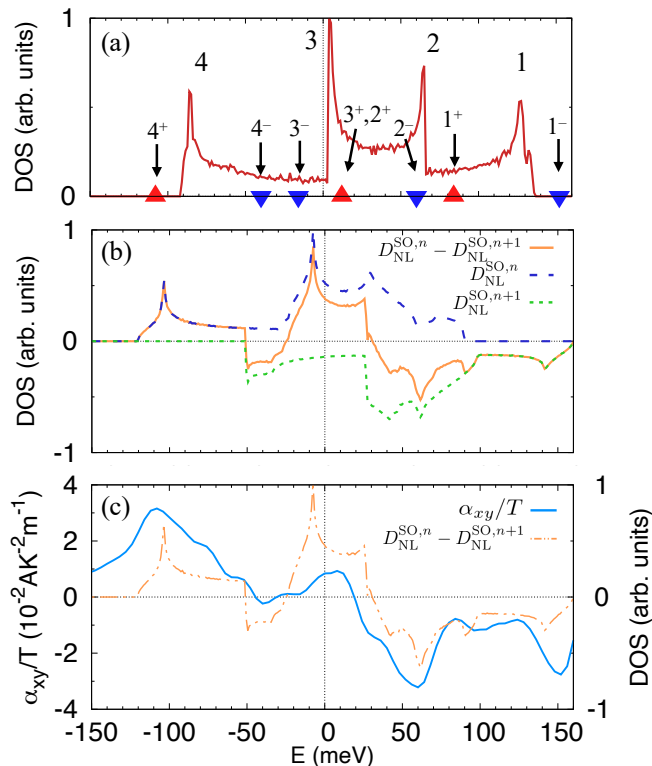


FIG. 4. (a) μ dependence of D_{NL} . The peaks 1, 2, 3, and 4 denote E_{VHS} . Solid upper (lower) triangle shows the maximum (minimum) in α_{xy}/T . Each value of energies is tabulated in Tab. II. (b) μ dependence of D_{NL} with SOC. Solid, dashed, dotted line are $D_{NL}^{SO,n} - D_{NL}^{SO,n+1}$, $D_{NL}^{SO,n}$, and $-D_{NL}^{SO,n+1}$ in eq. (10), respectively. (c) μ dependence of α_{xy}/T and $D_{NL}^{SO,n} - D_{NL}^{SO,n+1}$. Solid line is the results for $T = 30 \text{ K}$. Dashed double-dotted line shows $D_{NL}^{SO,n} - D_{NL}^{SO,n+1}$.

and E_{VHS} in D_{NL} more explicitly. The energy of the inflection point E_{IP} is estimated by taking the average of the energies at which α_{xy}/T takes its maximum and minimum and shows the breakdown of the Mott relation. While there is some deviation $\sim 10 \text{ meV}$ between these two characteristic energies, we see that the peak 1, 3, and 4 clearly correspond to E_{IP} . As for the origin of the deviation, we should note that E_{VHS} in D_{NL} is determined by a calculation without SOC. While the correspondence is not so clear for peak 2 (which is due to the presence of the Weyl points at $\sim 60 \text{ meV}^{21}$), we can conclude that a divergence in D_{NL} enhances α_{xy}/T and causes the breakdown of the Mott relation.

While we have seen that α_{xy}/T is always enhanced when μ is located around peaks of $D_{NL}^{SO,n+1}$ ($D_{NL}^{SO,n}$), it is difficult to predict the absolute value of α_{xy}/T by just looking at the value of D_{NL} . For example, although peak 3 in D_{NL} is higher than peak 2 (Fig. 3(b)), the absolute value of α_{xy}/T at 64 meV (which corresponds to peak 2) is larger than that at 12 meV (which corresponds to peak 3). This is because the averaged Ω_{NL}^n (eq. (9)) in peak 2 is larger than that in peak 3. As is mentioned above, it

TABLE II. One-to-one correspondence between the peaks in D_{NL} and E_{IP} in $\text{Co}_3\text{Sn}_2\text{S}_2$. E_{IP} is estimated as an average of energy taking the maximum and minimum in α_{xy}/T . $\alpha_{xy}^{+(-)}/T$ denotes the energy at which α_{xy}/T takes its maximum (minimum) and deviates from the Mott relation.

Peak	D_{NL} (meV)	E_{IP} (meV)	α_{xy}^+/T (meV)	α_{xy}^-/T (meV)
1	126	118	84	152
2	62	36	12	60
3	3	-2	12	-16
4	-88	-74	-108	-40

has been shown that there are Weyl points at $\sim 60 \text{ meV}$, which generally make Ω_{NL}^n larger²¹.

C. Magnetic Weyl semimetal Co_2MnGa

Next, let us investigate the case of another prototypical magnetic Weyl semimetal Co_2MnGa , for which a large ANE has been recently discovered¹⁸. Figure 5 shows the band structure, μ dependence of σ_{xy} and α_{xy}/T , and T dependence of α_{xy}/T . Here we assume that the direction of the magnetization is parallel to the [001] axis. The total magnetic moment is estimated to be $4.2 \mu_B/\text{f.u.}$, while the local magnetic moment of Mn and Co are 2.9 and 0.6 μ_B/atom , respectively. The calculated value of σ_{xy} at E_F ($1609 \Omega^{-1} \text{cm}^{-1}$) and the μ dependence of σ_{xy} (Fig. 5(b)) are consistent with the previous study.¹⁸ We see in Figs. 5(c) and (d) that there are several characteristic energies (20, -6, -62, -79 and -151 meV) for μ at which the absolute value of α_{xy} is significantly enhanced and the α_{xy}/T show a peculiar T dependence (i.e., the Mott relation is violated). As we will see below, these characteristic energies can be understood in terms of the peaks in D_{NL} . Note that since there are five peaks in D_{NL} within a narrow energy range, some of maximum and minimum points in α_{xy}/T are degenerated.

As has been pointed out by previous studies^{18,19,50}, in the low energy band structure of Co_2MnGa , there are several topological objects such as the Hopf link of nodal lines and type-II Weyl points. On the other hand, we are interested in the stationary points in the dispersion of the nodal lines and the relation between their energies (E_{VHS} 's) and the characteristic energies for α_{xy}/T . Among many nodal lines, we look into the crossing between the same spin bands. It should be noted that the effect of SOC on the crossing between the opposite spin bands is usually weak when the exchange splitting is sufficiently large. Thus the Berry curvature is expected to be large along the nodal lines made from the parallel spins. In the following, we examine the two nodal lines formed by the three bands indicated in Fig. 5(a).

In Figs. 6(a) and (c), we show the nodal line formed by band 1 and 2 in Fig. 5(a). From the plot of D_{NL} in Fig. 6(c), we see that the “band width” of this nodal line is about 180 meV, and there are four “van Hove

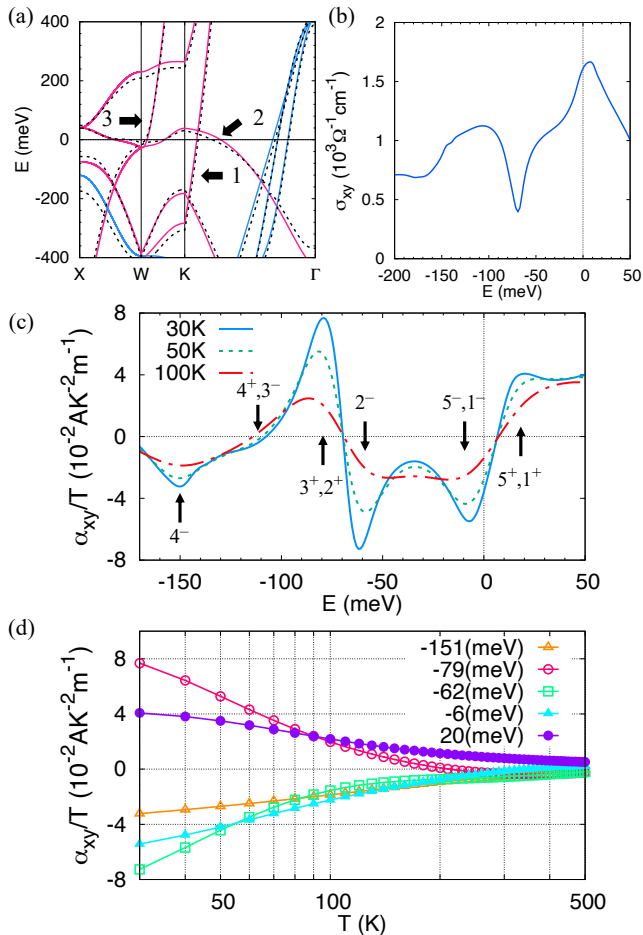


FIG. 5. (a) Band structure of Co_2MnGa . Pink and cyan lines correspond to up and down spin bands computed without SOC. Dashed lines show the band calculated including SOC. E_F and μ for the doped case are measured from the original Fermi level. The denoted majority bands 1, 2, and 3 make the nodal lines. (b) Chemical potential dependence of σ_{xy} at 0K. (c) Chemical potential dependence of α_{xy}/T . Solid, dotted, and dash-dotted line are the results for $T = 30, 50,$ and 100 K, respectively. The denoted numbers and superscripts identify the peaks and maximum or minimum in α_{xy}/T at which the Mott relation is violated, respectively. Each value of energies is tabulated in Tab. III. (d) Temperature dependence of α_{xy}/T . Lines with open triangle, open circle, open square, solid triangle, and solid circle correspond to the results for $\mu = -151, -79, -62, -6$ and $+20$ meV, respectively.

singularities” (indicated as peak 1, 2, 3, and 4) at 17, -58 , -85 , and -140 meV. We see that E_{VHS} is located between open-circle and solid-triangle points for which the Mott relation is violated. Interestingly, there is a clear one-to-one correspondence between these E_{VHS} ’s and E_{IP} ’s (see Table III)⁷². This result indicates that divergence in D_{NL} indeed characterizes the anomalous behavior of α_{xy} .

It should be noted that there are type-II Weyl points whose energies are close to peak 1. In the previous study

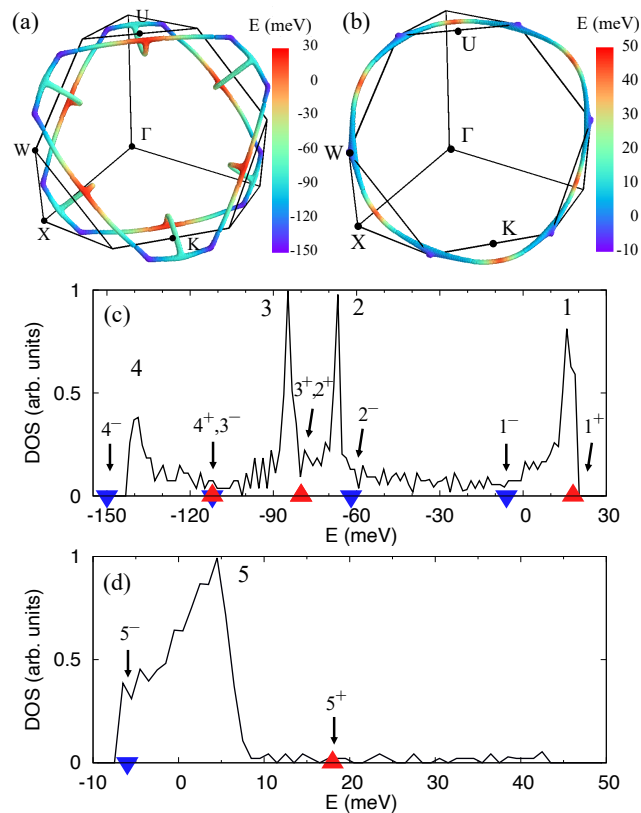


FIG. 6. (a)(b) Nodal line network of Co_2MnGa formed by band 1 and 2, and 2 and 3 in Fig. 5(a). The color bar corresponds to the energy range from -150 to 50 meV, and -10 to 50 meV. (c)(d) D_{NL} for the nodal line shown in (a)(b). The peak 1, 2, 3, 4 and 5 denotes E_{VHS} in D_{NL} . Solid upper (lower) triangle shows the maximum (minimum) in α_{xy}/T denoted in Fig. 5(c).

based on a model Hamiltonian¹⁸, it has been shown that α_{xy}/T shows a logarithmic divergence when the band dispersion around the Weyl points is flat and close to the transition between type-I and type-II. This result is consistent with our present argument based on the divergence in D_{NL} .

Next, let us look into the nodal line formed by band 2 and 3 shown in Figs. 6(b) and (d). The “band width” of this nodal line is just 60 meV, which is about one-third of that of the nodal line shown in Fig. 6(a). We see that there is a peak in D_{NL} (peak 5 in Fig. 6(d)) around 0 meV. This peak corresponds to the anomaly in α_{xy}/T at $\mu = -6$ and 18 meV (see Table III). While this nodal line has not been discussed in the previous study¹⁸, our present result suggests that hole-doping could be used to realize a large ANE in Co_2MnGa .

D. Ferromagnetic Heusler compound Fe_3Al

Let us finally move on to the D0_3 -type Heusler compound Fe_3Al . Recently, a large ANE has been discovered

TABLE III. One-to-one correspondence between the peaks in D_{NL} and E_{IP} in Co_2MnGa . E_{IP} is estimated as an average of energy taking the maximum and minimum in α_{xy}/T . $\alpha_{xy}^{+(-)}/T$ denotes the energy at which α_{xy}/T takes its maximum (minimum) and deviates from the Mott relation.

Peak	D_{NL} (meV)	E_{IP} (meV)	α_{xy}^+/T (meV)	α_{xy}^-/T (meV)
1	17	6	-6	18
2	-68	-71	-80	-62
3	-85	-96	-112	-80
4	-140	-131	-150	-112
5	4	6	-6	18

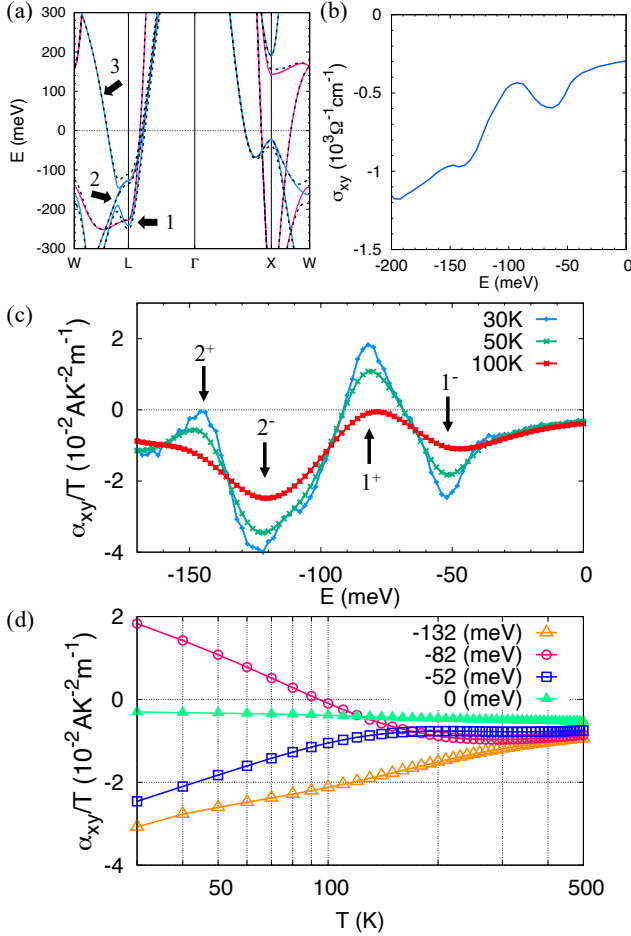


FIG. 7. (a) Band structure of Fe_3Al . Pink and cyan lines correspond to the majority and minority spin bands computed without SOC. Dashed lines show the bands calculated including SOC. The denoted minority bands 1, 2, and 3 make the nodal lines. (b) Energy dependence of σ_{xy} at 0K. (c) μ dependence of α_{xy}/T . Solid, dotted, and dash-dotted line are the results for $T = 30, 50,$ and 100K , respectively. The denoted number and superscripts identify the peaks and maximum or minimum in α_{xy}/T at which the Mott relation is violated, respectively. Each value of energies is tabulated in Tab. IV. (d) T dependence of α_{xy}/T . Lines with open triangle, open circle, open square, and solid triangle correspond to the results for $\mu = -132, -82, -52,$ and $+0$ meV, respectively.

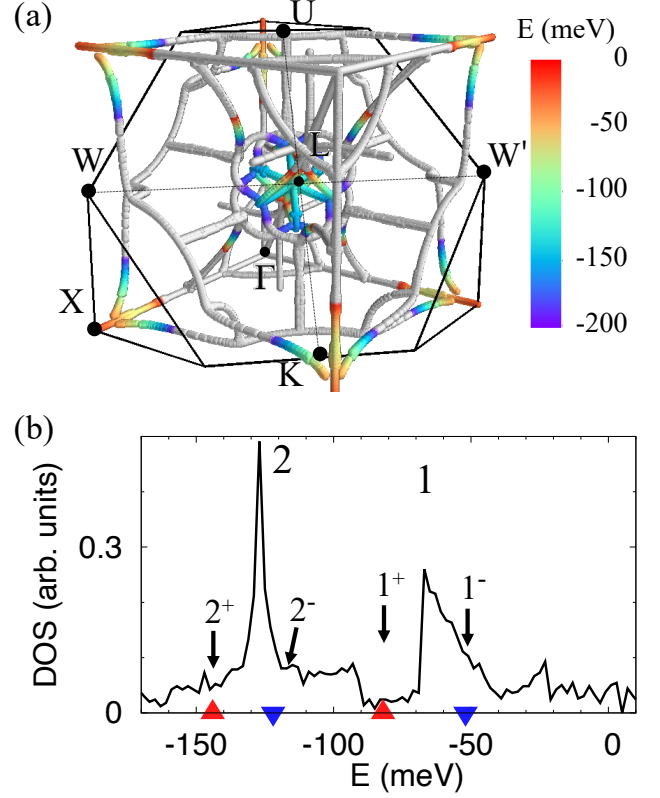


FIG. 8. (a) Nodal line network of Fe_3Al . The color bar corresponds to the energy range from -200 to 0 meV. The gray part in the main figure denotes that the energy is the outside of the range of the color bar. (b) Density of states projected onto the nodal lines. The denoted peaks 1, 2, and 3 show the E_{VHS} in the D_{NL} . Solid upper (lower) triangle shows the maximum (minimum) in α_{xy}/T denoted in Fig. 7(c).

in Fe_3X ($X=\text{Al}, \text{Ga}$) for which the nodal lines around L point has been shown to play a crucial role²⁰. In the following, we focus on Fe_3Al and show that the enhancement of the transverse TE conductivity and the violation of the Mott relation can be understood in terms of E_{VHS} .

Figure 7 shows the band structure, μ dependence of σ_{xy} and α_{xy}/T , and T dependence of α_{xy}/T . Here we assume that the direction of the magnetization is along the $[001]$ axis. Regarding the atomic positions of Fe atoms, there are two types of sites Fe(I) and Fe(II). For the former, Fe atoms are surrounded by other eight Fe atoms forming a cube. For the latter, Fe atoms are surrounded by other four Fe atoms and four Al atoms forming a tetrahedron. The obtained total magnetic moment is $5.93 \mu_B/\text{f.u.}$; the local magnetic moments of Fe(I), Fe(II), and Al are $2.5, 1.9,$ and $-0.3 \mu_B/\text{atom}$, respectively. These results agree well with the previous experimental and theoretical results.^{73,74}

While σ_{xy} is just $-285 \Omega^{-1}\text{cm}^{-1}$ and its absolute value is much smaller than those of Co_2MnGa and $\text{Co}_3\text{Sn}_2\text{S}_2$, σ_{xy} reaches $\sim -1000 \Omega^{-1}\text{cm}^{-1}$ when $\mu \sim -150$ meV (see Fig.7(b)). Since μ dependence of σ_{xy} is so drastic, we ex-

TABLE IV. One-to-one correspondence between the peaks in D_{NL} and E_{IP} in Fe_3Al . E_{IP} is estimated as an average of energy taking the maximum and minimum in α_{xy}/T . $\alpha_{xy}^{+(-)}/T$ denotes the energy at which α_{xy}/T takes its maximum (minimum) and deviates from the Mott relation.

Peak	D_{NL} (meV)	E_{IP} (meV)	α_{xy}^+/T (meV)	α_{xy}^-/T (meV)
1	-68	-67	-82	-52
2	-129	-133	-144	-122

pect that the absolute value of α_{xy} is large. Indeed, Figs. 7(c) and (d) show that while α_{xy}/T does not sensitively depend on T for $\mu \sim 0$, α_{xy}/T is dramatically enhanced and the Mott relation breaks down for $\mu = -52, -82, -132$ and -144 meV.

If we look at the low-energy band structure in Fig. 7(a), we see that there are many band crossings. Among them, as in the case of Co_2MnGa , let us first focus on the nodal lines formed by the same spin bands. More specifically, we focus on the band 1, 2 and 3 and nodal lines formed by these bands.

Figures 8(a) and (b) show the nodal lines and D_{NL} . The nodal lines have a complex structure, which are mainly located near the high-symmetry lines such as Γ -X and Γ -L line. There are two peaks at -68 and -129 meV in D_{NL} (peak 1 and peak 2). Peak 1 (2) originates from the nodal line around the X (L) point. Especially, the Berry curvature is large around the L point, which is consistent with the previous results in Ref. [20].

In Table IV, we compare E_{VHS} in D_{NL} and E_{IP} estimated by the energies at which α_{xy}/T shows a significant enhancement and the Mott relation is violated. We see that there is a clear one-to-one correspondence between E_{VHS} and E_{IP} . This result indicates again that the divergence in D_{NL} generally provides useful information to search for the energy at which α_{xy}/T enhances dramati-

cally.

IV. CONCLUSION

In summary, to investigate the origin of the enhancement of the transverse TE conductivity (α) in ferromagnets, we performed a systematic analysis for $\text{Co}_3\text{Sn}_2\text{S}_2$, Co_2MnGa and Fe_3Al , for which a large ANE has been recently discovered. α is directly related to the sum of the Berry curvature of the bands near the Fermi level. The intensity of the Berry curvature takes a large value along the nodal line, which is gapless in the non-relativistic calculation. Thus the DOS projected onto the nodal line (D_{NL}) gives a useful information to enhance α_{ij} . Since the nodal lines are one-dimensional objects, the stationary points in the nodal line makes a sharp ‘‘van Hove singularities’’ in D_{NL} . When the chemical potential is close to these singularities, α_{ij} is dramatically enhanced. In this situation, the Mott relation breaks down and α_{ij}/T shows a peculiar temperature dependence. We conclude that stationary points in the nodal lines or singularities in D_{NL} provide a useful guide to design magnetic materials with a large ANE.

ACKNOWLEDGMENTS

This work was supported by CREST (JPMJCR18T3, JPMJCR15Q5), by JSPS Grant-in-Aid for Scientific Research on Innovative Areas (JP18H04481 and JP19H05825), by Grants-in-Aid for Scientific Research (JP16H06345, JP16K04875, 19H00650, 20K14390) from JSPS, and by MEXT as a social and scientific priority issue (Creation of new functional devices and high-performance materials to support next-generation industries) to be tackled by using post-K computer (hp180206 and hp190169). The computations in this research were performed using the supercomputers at the ISSP, University of Tokyo.

* minami@cphys.s.kanazawa-u.ac.jp

† fishii@mail.kanazawa-u.ac.jp

¹ D. Xiao, Y. Yao, Z. Fang, and Q. Niu, Phys. Rev. Lett. **97**, 026603 (2006).

² N. Nagaosa, J. Sinova, S. Onoda, A. H. MacDonald, and N. P. Ong, Rev. Mod. Phys. **82**, 1539 (2010).

³ D. Xiao, M.-C. Chang, and Q. Niu, Rev. Mod. Phys. **82**, 1959 (2010).

⁴ Y. Sakuraba, Scripta Mater. **111**, 29 (2016).

⁵ M. Mizuguchi and S. Nakatsuji, Sci. Tech. Adv. Mater **20**, 262 (2019).

⁶ T. Jungwirth, Q. Niu, and A. H. MacDonald, Phys. Rev. Lett. **88**, 207208 (2002).

⁷ Q. Wang, Y. Xu, R. Lou, Z. Liu, M. Li, Y. Huang, D. Shen, H. Weng, S. Wang, and H. Lei, Nat. Commun. **9**, 4212

(2018).

⁸ S. Ouardi, G. H. Fecher, C. Felser, and J. Kübler, Phys. Rev. Lett. **110**, 100401 (2013).

⁹ A. K. Nayak, J. E. Fischer, Y. Sun, B. Yan, J. Karel, A. C. Komarek, C. Shekhar, N. Kumar, W. Schnelle, J. Kübler, C. Felser, and S. S. P. Parkin, Sci. Adv. **2**, e1501870 (2016).

¹⁰ T. Suzuki, R. Chisnell, A. Devarakonda, Y.-T. Liu, W. Feng, D. Xiao, J. Å. W. Lynn, and J. Å. G. Checkelsky, Nat. Phys. **12**, 1119 (2016).

¹¹ S. Nakatsuji, N. Kiyohara, and T. Higo, Nature **527**, 212 (2015).

¹² N. Kiyohara, T. Tomita, and S. Nakatsuji, Phys. Rev. Applied **5**, 064009 (2016).

¹³ H. Chen, Q. Niu, and A. H. MacDonald, Phys. Rev. Lett. **112**, 017205 (2014).

- ¹⁴ J.-C. Tung and G.-Y. Guo, *New J. Phys.* **15**, 033014 (2013).
- ¹⁵ Y. Yao, L. Kleinman, A. H. MacDonald, J. Sinova, T. Jungwirth, D.-s. Wang, E. Wang, and Q. Niu, *Phys. Rev. Lett.* **92**, 037204 (2004).
- ¹⁶ K. Manna, L. Muechler, T.-H. Kao, R. Stinshoff, Y. Zhang, J. Gooth, N. Kumar, G. Kreiner, K. Koepernik, R. Car, J. Kübler, G. H. Fecher, C. Shekhar, Y. Sun, and C. Felser, *Phys. Rev. X* **8**, 041045 (2018).
- ¹⁷ P. Li, J. Koo, W. Ning, J. Li, L. Miao, L. Min, Y. Zhu, Y. Wang, N. Alem, C.-X. Liu, Z. Mao, and B. Yan, *Nat. Commun.* **11**, 3476 (2020).
- ¹⁸ A. Sakai, Y. Mizuta, A. Nugroho, R. Sihombing, T. Koretsune, M. Suzuki, N. Takemori, R. Ishii, D. Nishio-Hamane, R. Arita, P. Goswami, and S. Nakatsuji, *Nat. Phys.* **14**, 1119 (2018).
- ¹⁹ S. N. Guin, K. Manna, J. Noky, S. J. Watzman, C. Fu, N. Kumar, W. Schnelle, C. Shekhar, Y. Sun, J. Gooth, and C. Felser, *NPG Asia Mater.* **11**, 16 (2019).
- ²⁰ A. Sakai, S. Minami, T. Koretsune, T. Chen, T. Higo, Y. Wang, T. Nomoto, M. Hirayama, S. Miwa, D. Nishio-Hamane, F. Ishii, R. Arita, and S. Nakatsuji, *Nature* **581**, 53 (2020).
- ²¹ E. Liu, Y. Sun, N. Kumar, L. Muechler, A. Sun, L. Jiao, S.-Y. Yang, D. Liu, A. Liang, Q. Xu, J. Kroder, V. Süß, H. Borrmann, C. Shekhar, Z. Wang, C. Xi, W. Wang, W. Schnelle, S. Wirth, Y. Chen, S. T. B. Goennenwein, and C. Felser, *Nat. Phys.* **14**, 1125 (2018).
- ²² H. Yang, W. You, J. Wang, J. Huang, C. Xi, X. Xu, C. Cao, M. Tian, Z.-A. Xu, J. Dai, and Y. Li, *Phys. Rev. Materials* **4**, 024202 (2020).
- ²³ S. N. Guin, P. Vir, Y. Zhang, N. Kumar, S. J. Watzman, C. Fu, E. Liu, K. Manna, W. Schnelle, J. Gooth, C. Shekhar, Y. Sun, and C. Felser, *Adv. Mater.* **31**, 1806622 (2019).
- ²⁴ Y. P. Mizuta, H. Sawahata, and F. Ishii, *Phys. Rev. B* **98**, 205125 (2018).
- ²⁵ G.-Y. Guo and T.-C. Wang, *Phys. Rev. B* **96**, 224415 (2017).
- ²⁶ Z. Shi, S.-J. Xu, L. Ma, S.-M. Zhou, and G.-Y. Guo, *Phys. Rev. Applied* **13**, 054044 (2020).
- ²⁷ S. Minami, F. Ishii, Y. P. Mizuta, and M. Saito, *Appl. Phys. Lett.* **113**, 032403 (2018).
- ²⁸ J. Xu, W. A. Phelan, and C.-L. Chien, *Nano Lett.* **19**, 8250 (2019).
- ²⁹ J. Noky, Q. Xu, C. Felser, and Y. Sun, *Phys. Rev. B* **99**, 165117 (2019).
- ³⁰ K. Hasegawa, M. Mizuguchi, Y. Sakuraba, T. Kamada, T. Kojima, T. Kubota, S. Mizukami, T. Miyazaki, and K. Takanashi, *Appl. Phys. Lett.* **106**, 252405 (2015).
- ³¹ W.-L. Lee, S. Watauchi, V. L. Miller, R. J. Cava, and N. P. Ong, *Phys. Rev. Lett.* **93**, 226601 (2004).
- ³² T. Miyasato, N. Abe, T. Fujii, A. Asamitsu, S. Onoda, Y. Onose, N. Nagaosa, and Y. Tokura, *Phys. Rev. Lett.* **99**, 086602 (2007).
- ³³ Y. Pu, D. Chiba, F. Matsukura, H. Ohno, and J. Shi, *Phys. Rev. Lett.* **101**, 117208 (2008).
- ³⁴ S. Y. Huang, W. G. Wang, S. F. Lee, J. Kwo, and C. L. Chien, *Phys. Rev. Lett.* **107**, 216604 (2011).
- ³⁵ M. Ikhlas, T. Tomita, T. Koretsune, M.-T. Suzuki, D. Nishio-Hamane, R. Arita, Y. Otani, and S. Nakatsuji, *Nat. Phys.* **13**, 1085 (2017).
- ³⁶ Y. Sakuraba, K. Hasegawa, M. Mizuguchi, T. Kubota, S. Mizukami, T. Miyazaki, and K. Takanashi, *Appl. Phys. Express* **6**, 033003 (2013).
- ³⁷ R. Syariati, S. Minami, H. Sawahata, and F. Ishii, *APL Materials* **8**, 041105 (2020).
- ³⁸ H. Nakayama, K. Masuda, J. Wang, A. Miura, K.-i. Uchida, M. Murata, and Y. Sakuraba, *Phys. Rev. Materials* **3**, 114412 (2019).
- ³⁹ L. Muechler, E. Liu, J. Gayles, Q. Xu, C. Felser, and Y. Sun, *Phys. Rev. B* **101**, 115106 (2020).
- ⁴⁰ Y. Chen, Y. Xie, S. A. Yang, H. Pan, F. Zhang, M. L. Cohen, and S. Zhang, *Nano Lett.* **15**, 6974 (2015).
- ⁴¹ H. Weng, Y. Liang, Q. Xu, R. Yu, Z. Fang, X. Dai, and Y. Kawazoe, *Phys. Rev. B* **92**, 045108 (2015).
- ⁴² Y. Kim, B. J. Wieder, C. L. Kane, and A. M. Rappe, *Phys. Rev. Lett.* **115**, 036806 (2015).
- ⁴³ R. Yu, H. Weng, Z. Fang, X. Dai, and X. Hu, *Phys. Rev. Lett.* **115**, 036807 (2015).
- ⁴⁴ L. S. Xie, L. M. Schoop, E. M. Seibel, Q. D. Gibson, W. Xie, and R. J. Cava, *APL Materials* **3**, 083602 (2015).
- ⁴⁵ Y.-H. Chan, C.-K. Chiu, M. Y. Chou, and A. P. Schnyder, *Phys. Rev. B* **93**, 205132 (2016).
- ⁴⁶ A. Yamakage, Y. Yamakawa, Y. Tanaka, and Y. Okamoto, *J. Phys. Soc. Jpn.* **85**, 013708 (2016).
- ⁴⁷ M. Hirayama, R. Okugawa, T. Miyake, and S. Murakami, *Nat. Commun.* **8**, 14022 (2017).
- ⁴⁸ H. Huang, J. Liu, D. Vanderbilt, and W. Duan, *Phys. Rev. B* **93**, 201114 (2016).
- ⁴⁹ A. A. Soluyanov, D. Gresch, Z. Wang, Q. Wu, M. Troyer, X. Dai, and B. A. Bernevig, *Nature* **527**, 495 (2015).
- ⁵⁰ G. Chang, S.-Y. Xu, X. Zhou, S.-M. Huang, B. Singh, B. Wang, I. Belopolski, J. Yin, S. Zhang, A. Bansil, H. Lin, and M. Z. Hasan, *Phys. Rev. Lett.* **119**, 156401 (2017).
- ⁵¹ K. Manna, Y. Sun, L. Muechler, J. Kübler, and C. Felser, *Nat. Rev. Mater.* **3**, 244 (2018).
- ⁵² K. Kim, J. Seo, E. Lee, K. T. Ko, B. S. Kim, B. G. Jang, J. M. Ok, J. Lee, Y. J. Jo, W. Kang, J. H. Shim, C. Kim, H. W. Yeom, B. Il Min, B.-J. Yang, and J. S. Kim, *Nat. Mater.* **17**, 794 (2018).
- ⁵³ H. Hodovanets, C. J. Eckberg, P. Y. Zavalij, H. Kim, W.-C. Lin, M. Zic, D. J. Campbell, J. S. Higgins, and J. Paglione, *Phys. Rev. B* **98**, 245132 (2018).
- ⁵⁴ N. Kanazawa, K. Shibata, and Y. Tokura, *New J. Phys* **18**, 045006 (2016).
- ⁵⁵ D. Destraz, L. Das, S. S. Tsirkin, Y. Xu, T. Neupert, J. Chang, A. Schilling, A. G. Grushin, J. Kohlbrecher, L. Keller, P. Puphal, E. Pomjakushina, and J. S. White, *npj Quantum Mater.* **5**, 5 (2020).
- ⁵⁶ J. M. Ziman, *Principles of the Theory of Solids*, 2nd ed. (Cambridge University Press, 1972).
- ⁵⁷ N. Mott and H. Jones, *The theory of the properties of metals and alloys*, Dover books on physics (Dover Publications, 1958).
- ⁵⁸ M. Jonson and G. D. Mahan, *Phys. Rev. B* **21**, 4223 (1980).
- ⁵⁹ M. Cutler and N. F. Mott, *Phys. Rev.* **181**, 1336 (1969).
- ⁶⁰ Y. Wang, Z. A. Xu, T. Kakeshita, S. Uchida, S. Ono, Y. Ando, and N. P. Ong, *Phys. Rev. B* **64**, 224519 (2001).
- ⁶¹ N. Hanasaki, K. Sano, Y. Onose, T. Ohtsuka, S. Iguchi, I. Kézsmárki, S. Miyasaka, S. Onoda, N. Nagaosa, and Y. Tokura, *Phys. Rev. Lett.* **100**, 106601 (2008).
- ⁶² P. Webster, *J. Phys. Chem. Solids* **32**, 1221 (1971).
- ⁶³ P. Vaquero and G. G. Sobany, *Solid State Sci.* **11**, 513 (2009).
- ⁶⁴ Y. Nishino, M. Kato, S. Asano, K. Soda, M. Hayasaki, and U. Mizutani, *Phys. Rev. Lett.* **79**, 1909 (1997).

- ⁶⁵ J. Kubler, K. H. Hock, J. Sticht, and A. R. Williams, *J. Phys. F* **18**, 469 (1988).
- ⁶⁶ Openmx: Open source package for material explorer, <http://www.openmx-square.org/>.
- ⁶⁷ I. Morrison, D. M. Bylander, and L. Kleinman, *Phys. Rev. B* **47**, 6728 (1993).
- ⁶⁸ G. Theurich and N. A. Hill, *Phys. Rev. B* **64**, 073106 (2001).
- ⁶⁹ T. Ozaki, *Phys. Rev. B* **67**, 155108 (2003).
- ⁷⁰ Q. Wu, S. Zhang, H.-F. Song, M. Troyer, and A. A. Soluyanov, *Comput. Phys. Commun* **224**, 405 (2018).
- ⁷¹ G. Pizzi, V. Vitale, R. Arita, S. Blügel, F. Freimuth, G. Géranton, M. Gibertini, D. Gresch, C. Johnson, T. Koretsune, J. Ibañez-Azpiroz, H. Lee, J.-M. Lihm, D. Marchand, A. Marrazzo, Y. Mokrousov, J. I. Mustafa, Y. Nohara, Y. Nomura, L. Paulatto, S. Poncé, T. Ponweiser, J. Qiao, F. Thöle, S. S. Tsirkin, M. Wierzbowska, N. Marzari, D. Vanderbilt, I. Souza, A. A. Mostofi, and J. R. Yates, *J. Phys. Condens. Matter* **32**, 165902 (2020).
- ⁷² Note that D_{NL} is calculated without considering SOC, so that the peaks in D_{NL} do not coincide perfectly with E_{IP} due to the SOC gap.
- ⁷³ T. J. Burch, K. Raj, P. Jena, J. I. Budnick, V. Niculescu, and W. B. Muir, *Phys. Rev. B* **19**, 2933 (1979).
- ⁷⁴ B. Xu, J. Liu, and L. Yi, *Phys. Lett. A* **363**, 312 (2007).